PROCEEDINGS OF SPIE

SPIEDigitalLibrary.org/conference-proceedings-of-spie

H2RG detector characterization for RIMAS and instrument efficiencies

Vicki L. Toy, Alexander S. Kutyrev, John I. Capone, Thomas Hams, F. David Robinson, et al.

Vicki L. Toy, Alexander S. Kutyrev, John I. Capone, Thomas Hams, F. David Robinson, Gennadiy N. Lotkin, Sylvain Veilleux, Samuel H. Moseley, Neil A. Gehrels, Stuart N. Vogel, "H2RG detector characterization for RIMAS and instrument efficiencies," Proc. SPIE 9908, Ground-based and Airborne Instrumentation for Astronomy VI, 99083I (9 August 2016); doi: 10.1117/12.2230181

SPIE.

Event: SPIE Astronomical Telescopes + Instrumentation, 2016, Edinburgh, United Kingdom

H2RG detector characterization for RIMAS and instrument efficiencies

Vicki L. Toy[a], Alexander S. Kutyrev[a,b], John I. Capone[a],
Thomas Hams[b], F. David Robinson[b], Gennadiy N. Lotkin[b],
Sylvain Veilleux[a,c], Samuel H. Moseley[b], Neil A. Gehrels[b], Stuart N. Vogel[a]

[a]University of Maryland, College Park, Department of Astronomy, College Park, MD, USA 20742; [b]NASA Goddard Space Flight Center, 8800 Greenbelt Rd., Greenbelt, MD, USA 20771; [c] Joint Space-Science Institute, University of Maryland, College Park, MD 20742, USA

ABSTRACT

The Rapid infrared IMAger-Spectrometer (RIMAS) is a near-infrared (NIR) imager and spectrometer that will quickly follow up gamma-ray burst afterglows on the 4.3-meter Discovery Channel Telescope (DCT). RIMAS has two optical arms which allows simultaneous coverage over two bandpasses (YJ and HK) in either imaging or spectroscopy mode. RIMAS utilizes two Teledyne HgCdTe H2RG detectors controlled by Astronomical Research Cameras, Inc. (ARC/Leach) drivers. We report the laboratory characterization of RIMAS's detectors: conversion gain, read noise, linearity, saturation, dynamic range, and dark current. We also present RIMAS's instrument efficiency from atmospheric transmission models and optics data (both telescope and instrument) in all three observing modes.

Keywords: detectors, RIMAS, photometry, GRB, infrared, efficiency, H2RG, HXRG

1. INTRODUCTION

The Rapid infrared IMAger-Spectrometer (RIMAS) is a rapid, near-infrared, cryogenic instrument designed to follow up high-redshift gamma-ray burst (GRB) afterglows from the 4.3-meter Discovery Channel Telescope (DCT). RIMAS is being built at NASA Goddard Space Flight Center (GSFC) in collaboration with the University of Maryland, College Park (UMCP) and Lowell Observatory. The instrument will be one of five instruments permanently installed on the "instrument" cube on the DCT. RIMAS covers $0.97 - 2.39\mu m$ and can operate in photometric imaging, low-resolution spectroscopy (R≈30), or high-resolution spectroscopy (R≈4000) observing mode.

The primary science motivation for RIMAS is to follow up *Swift* Observatory triggered GRBs from the ground. RIMAS is designed to be a rapid follow up instrument due to the rapidly fading nature of GRB afterglows. This is accomplished by switching between the instruments on the DCT by inserting a mirror or dichroic beam splitter into the beam in the instrument cube. Additionally, RIMAS separates light into two optical arms (YJ and HK) with a dichroic beam splitter which allows simultanous coverage in both photometry and spectroscopy modes. Each optical arm contains a camera and a science grade Teledyne HgCdTe Astronomy Wide Area Infrared Imager with 2K x 2K, Reference Pixels and Guide Mode (H2RG) detector.[1] RIMAS also has a slit-viewing camera (with near-infrared InSb detector) to guide on the slit during spectroscopy mode.

RIMAS is currently in the integration phase and Figure 1 shows the current status of RIMAS. The major components of the main dewar are in place (note that there will be a second filter wheel installed at a later date) and we aim to commission on the DCT in Winter 2016.

We report the detector characterization of the two RIMAS H2RG detectors from laboratory results. This information will be incorporated into RIMAS's automatic data reduction pipeline. We also report instrument efficiencies for all three observing modes.

Author's e-mail: vtoy@astro.umd.edu

Ground-based and Airborne Instrumentation for Astronomy VI, edited by Christopher J. Evans, Luc Simard, Hideki Takami
Proc. of SPIE Vol. 9908, 99083I · © 2016 SPIE · CCC code: 0277-786X/16/$18 · doi: 10.1117/12.2230181

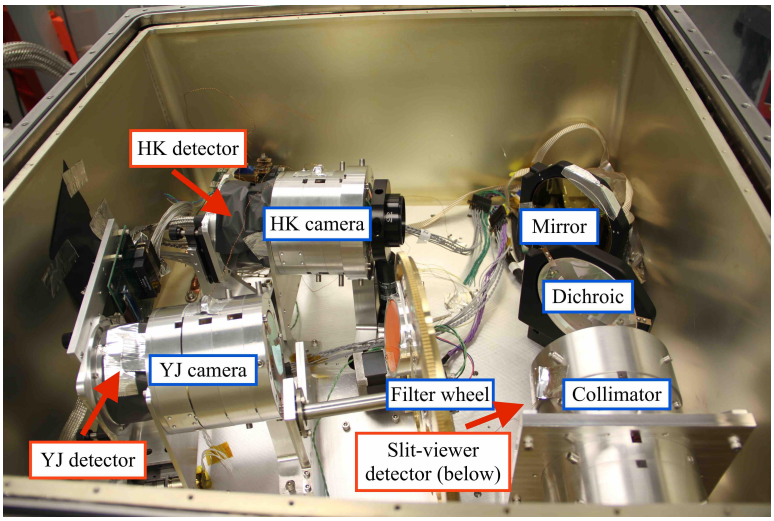

Figure 1. Inside RIMAS's dewar. The red labels point out RIMAS's three near-infrared detectors, while the blue labels show optical or mechanical components. Note that RIMAS will have a second filter wheel installed in front of the HK camera.

2. SET-UP

The RIMAS H2RG detectors (YJ detector - 1.7 μm, HK detector - 2.5μm) have pixel sizes of $18 \times 18 \mu m^2$ and are operated with two identical Astronomical Research Camera, Inc. (ARC/Leach) controllers. Each detector has a separate PCI driver card on the detector control computer and can be run separately or simultaneously. The detector driver set-up and slit-viewer detector characterization are described in detail in previous conference proceedings.[2] We run our detectors in 32-channel buffered mode at 100kHz and acquire frames in up-the-ramp (UTR) sampling mode with a minimum exposure time of 500ms. The programmable analog-to-digital converter (ADC) offsets are set such that the reference pixels are at the same level across the detector.

We have operated the H2RG detectors at room temperature for optical alignment verification, but only report detector characterization data at 60-85K.

3. H2RG CHARACTERIZATION

We report the laboratory characterization of the RIMAS detectors at cryogenic temperatures: conversion gain, read noise, linearity, saturation, dynamic range, and dark current. The results are summarized in Table 1 and the analysis is explained in detail in the remainder of this section.

3.1 Conversion Gain

We measured the conversion gain with an LED source outside the dewar window with diffusers to create a uniform source of illumination. The six datasets are taken with UTR of 128 and exposure time of 500ms with filters in front of the detectors.

We use the photon transfer technique to measure the conversion gain. This is done by measuring the slope of the variance against the median signal. We subtract the first frame from all subsequent frames in each dataset, then subtract frame-by-frame another dataset; this removes any large source variation. We note that we see low levels of non-uniformity (after subtracting another dataset) because the source is not perfectly uniform. In order to mitigate this effect we only use a small 100x100 pixel box near the center of the detector to calculate the conversion gain.

We calculate the variance in the difference frame, corrected for a factor of four due to the increase in noise from subtracting both the first frame and the frame from ther other dataset, and median signal. The conversion gain for both H2RG detectors is shown in Figure 2. Note that in Figure 2 the conversion gain (inverse slope)

Table 1. Detector characteristics

Characteristics	YJ Detector	HK Detector
Conversion gain (e^-/ADU)	8.15 ± 0.12	8.82 ± 0.06
[a]Read noise (e^-)	13.20 ± 0.19	10.87 ± 0.07
Saturation (ADU)	37,725	32,467
Dynamic range (dB)	43.7	44.2
[b]Dark Current (e^-/s)	0.41	0.15

[a]Read noise reported for Fowler 16 and error from conversion gain.
[b]Needs to be retested with baffles and will replace YJ detector due to large dark current ramp.

starts to drift at larger median signals. This is likely due to the non-uniformity of the source becoming more significant with larger signal; however, the deviation is $< 7\%$ which indicates this is a minor non-uniformity. We mitigate this effect by only using the first five points (where the slope is linear). We perform a linear regression over five difference datasets and report the gain conversion in Table 1.

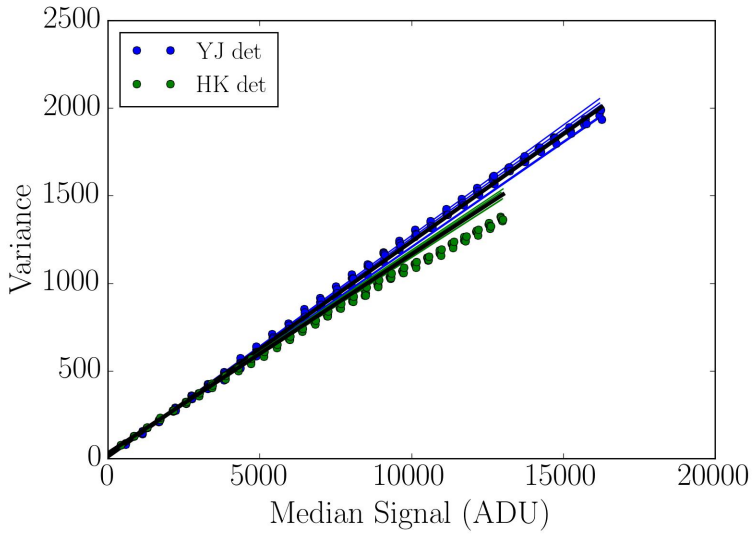

Figure 2. Conversion gain for both detectors from 100x100 pixel boxes near the center of the detectors. Note the drift from linearity at higher signals is likely due to small non-uniformity in the signal becoming more significant with more signal. The largest deviation in the gain is $< 7\%$, but we only calculate the conversion gain from the lower signal region (first five datapoints) and fit all five difference datasets to avoid this non-uniformity.

3.2 Linearity and Saturation

In order to measure the linearity and saturation of our detectors, we place an LED source outside the dewar window with diffusers to create a uniform source of illumination. We use the same data as the conversion gain calculation (see §3.1). We use a single dataset and subtract the first frame from subsequent frames. Our analysis is limited to a 500x500 pixel box near the center of the detector to reduce signal variation. We perform a linear

regression for the first two datapoints on each pixel within the box to determine the bias voltage and offset each pixel by this amount to effectively force each pixel to start at 0 analog-to-digital unit (ADU). We then perform a second linear regression for the first six datapoints (this is within the linear regime for most pixels). The middle pixel of the 500x500 pixel box acts as a reference pixel and we scale the slopes of all other pixels to match this reference pixel; this corrects for different scaling factors between pixels. We plot the median signal in both ADUs and electrons (using the conversion gain in §3.1) for both detectors in Figure 3. The detectors start to deviate from linearity around ∼20,000 ADU.

For strong signals, the detectors become extremely non-linear. The point when adding more photons does not increase the number of ADUs read out is called saturation. At this point the potential well is full and we cannot accurately measure the flux of a source. The saturation point is different for each pixel so we take the last frame of a single UTR 128 dataset and subtract the first frame. We only look at the 500x500 pixel box we defined for our linearity measurements and fit a Gaussian function to a histogram of the signal in ADUs (see Figure 3). We report the saturation from the mean of the Gaussian fit in Table 1. We note that we see an increase in the saturation point at lower temperatures.

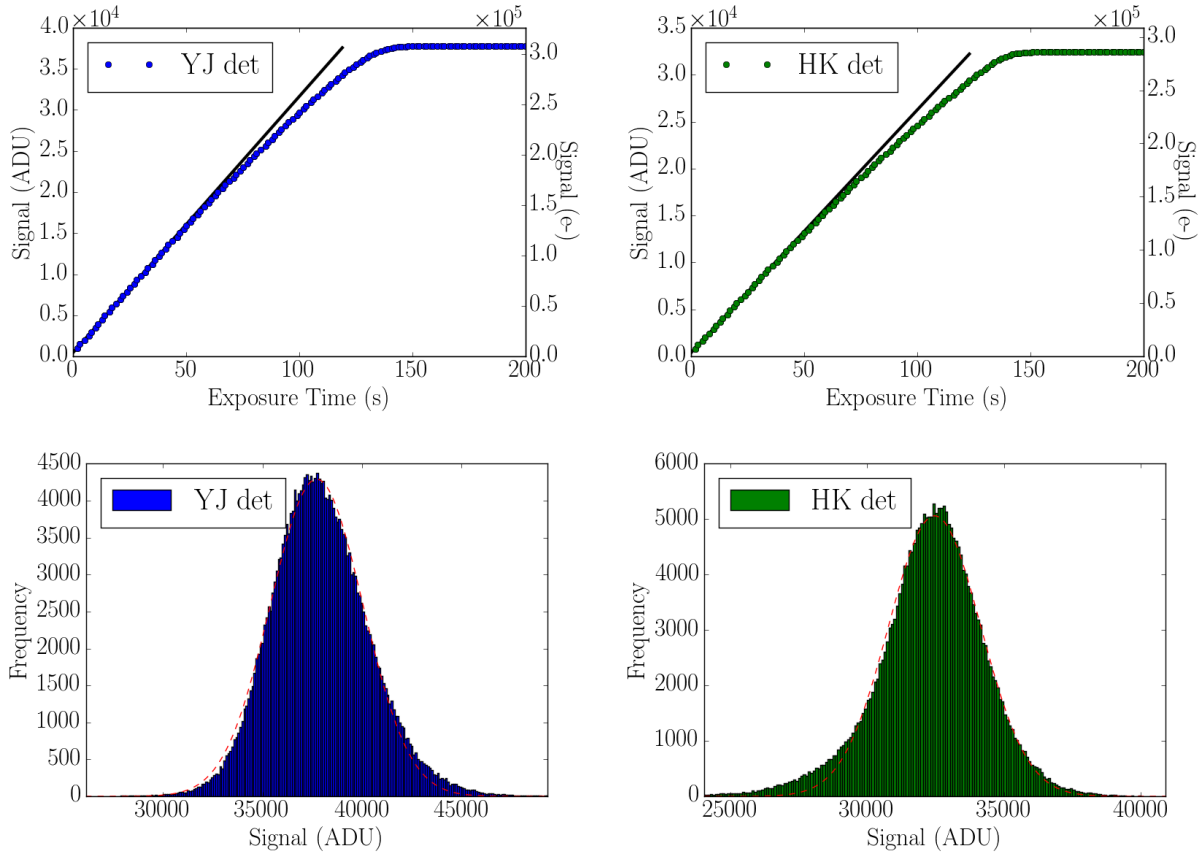

Figure 3. (*top*) Linearity of median of 500x500 pixel box for both detectors. Pixels have been corrected for bias voltages and different scaling factors between pixels. Black lines are linear fits to the first six frames. Detector starts to behave non-linearly around ∼20,000 ADU. (*bottom*) Saturation point of last frame for the 500x500 pixel box of the detector. We fit a Gaussian distribution (red) to get an estimate of the saturation point of the detectors.

3.3 Read noise

We calculate the read noise by measuring the variance of each pixel as a function of Fowler number while the detector is cold and dark. This is done by using two identical sets of data with UTR of 255 and exposure time of 500ms. We subtract one dataset from another to remove any residual light signal. We break the UTR 255

frames into Fowler sets of 1, 2, 4, 8, 16, and 32 using the first 2, 4, 8, 16, 32, and 64 frames respectively. We take the median of the pedestal frame per pixel and subtract it from the median in the signal frame per pixel. We perform a 3-σ clip on the data and calculate the variance across the difference frame, correcting the variance by a factor of four due to the increase of variance from subtracting two datasets and subtracting the pedestal frame. We report our H2RG detector read noise in Figure 4 and the read noise for Fowler 16 in Table 1. The increase in read noise for Fowler 64 and 128 is from the source noise dominating over the read noise.

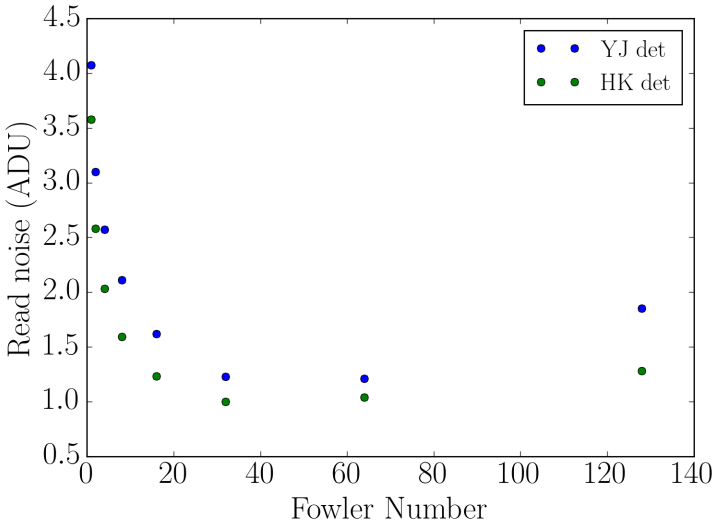

Figure 4. Read noise for YJ and HK detectors. The increase in read noise for Fowler 64 and 128 is from the source noise dominating over the read noise.

3.4 Dynamic Range

The dynamic range of a detector is set at the low end by the read noise and at the high end by the saturation. We report the dynamic range of both our detectors in Table 1 using our reported conversion gain.

3.5 Dark Current

We measure the dark current while the detector is cold and dark and use the same datasets as those used to calculate read noise in §3.3. We perform a linear regression on the reference pixels along the columns and subtract the fit from the entire array. This corrects for slowly varying electrical noise. The dark current is shown in Figure 5 and Table 1. Our dark current is fairly high for a typical H2RG (typical read noise is $\sim$0.005 e^-/s). We suspect that there may be a potential light leak that is scattering light into our detectors and we are currently working on installing baffles to reduce this light leak.

There is also a "ramp" in the dark current in Figure 5 in both detectors. In the HK detector this ramp was drastically reduced both in time and in amplitude by taking short exposure times (500ms) rather than long exposure times (10s). This may be due to the readout electronics cooling during exposure times because the clocks are not constantly running. We are investigating this problem and will install a heater controlled with a proportional-integral-derivative (PID) loop to regulate the detector temperature more precisely. The YJ detector, on the other hand, has a very large dark current ramp that is variable and is still problematic even with short exposure times. We believe this may be detector degradation from an known defect in the barrier layer of this batch of H2RG detectors.[3,4] This problem is more significant and will drastically impact faint and long exposure observations. We plan to replace this YJ detector in the future.

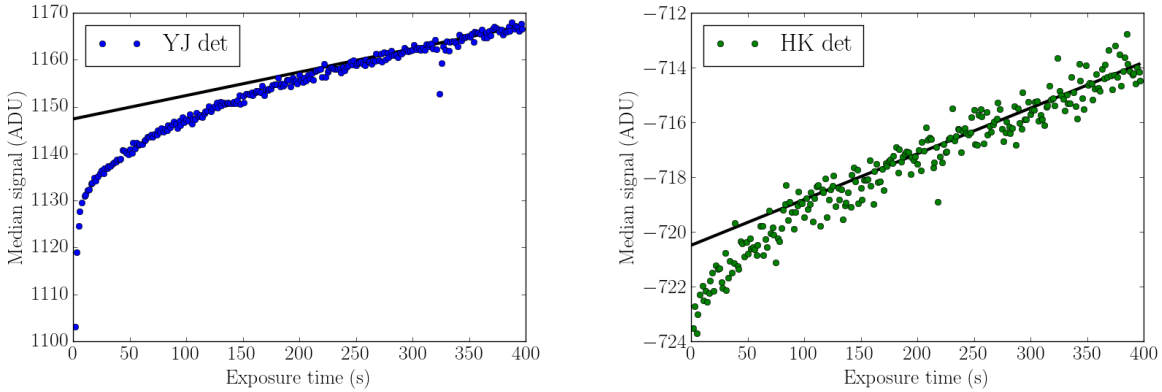

Figure 5. (*top*) Dark current for YJ detector (left) and HK detector (right). There are dark current ramps in both detectors, however, we find the ramp in the HK detector decreases with decreasing exposure times which indicates this may be from thermal instability of the detector. The YJ detector has a very non-linear ramp in the dark current that is likely due to detector degradation from a known problem with the barrier layer of this batch of detectors. We plan to replace the YJ detector.

4. INSTRUMENT EFFICIENCIES

We report total instrument efficiency in three separate modes. Following the light path we include (we report median efficiencies in parentheses and for spectroscopy we list the redder optical arm efficiency estimate first): (1) atmospheric transmission efficiencies from Kitt Peak[5] (∼96%), (2) reflection efficiencies from the telescope's primary and secondary mirrors (∼92%), (3) transmission efficiency estimates for the fold mirror/dichroic beam splitter in the center of the instrument cube (95%), (4) transmission efficiencies through windowed surfaces (∼90%), (5) slit transmission efficiencies for low- and high-resolution spectroscopy (50%), (6) transmission efficiencies through collimator (five AR coated lenses, ∼93%), (7) either reflection or transmission efficiencies through dichroic beam splitter (∼98%), (8) reflection efficiencies only for mirror on redder optical arm (95%), (9) transmission efficiencies through filter (for photometry, ∼90-98%), grating (for low-resolution spectroscopy, ∼64% and ∼63%), or cross-disperser+straightening prism+grating (for high-resolution spectroscopy, ∼53% and ∼34%) (10) transmission efficiencies through camera lenses (five AR coated lenses for each optical arm, ∼91%), and (12) estimated quantum efficiencies from science H2RG detectors (80%). The effective instrument photometric imaging, low-resolution spectroscopy, and high-resolution spectroscopy efficiencies are shown in Figure 6. The low-resolution spectroscopy efficiencies are still preliminary as the gratings are currently being ordered.

5. SUMMARY

We report the performance of the two H2RG detectors in RIMAS. The detectors use ARC/Leach controllers and we report the conversion gain, read noise, linearity, saturation, dynamic range, and dark current of these detectors. This data will be integrated into a user pipeline to reduce photometric and spectroscopic errors. Additionally we report total instrument efficiency in the three observing modes RIMAS will operate in. These values are used to create realistic limiting magnitude and exposure time calculators for RIMAS users. We will verify these models during commissioning on the DCT in Winter 2016.

6. ACKNOWLEDGMENTS

We would like to thank NASA Goddard's Detector Characterization Laboratory (DCL) for their time, expertise, and advice in running the HAWAII-2RG detectors, in particular Augustyn Waczynski. We also thank Chris Bebek for loaning RIMAS one of the SNAP HAWAII-2RG detectors. This work was supported by the National Aeronautics and Space Administration (NASA) Headquarters under the NASA Earth and Space Science Fellowship Program (Grant NNX12AL70H) to VT. VT, JC, and SV were partially supported by NSF/ATI grant 1207785.

REFERENCES

[1] Capone, J. I., Content, D. A., Kutyrev, A. S., Robinson, F. D., Lotkin, G. N., Toy, V. L., Veilleux, S., Moseley, S. H., Gehrels, N. A., and Vogel, S. N., "Cryogenic optical systems for the rapid infrared imager/spectrometer (RIMAS)," in [*Ground-based and Airborne Instrumentation for Astronomy V*], Proc. SPIE **9147**, 914736 (2014).

[2] Toy, V. L., Kutyrev, A. S., Lyness, E. I., Muench, M., Robinson, F. D., Lotkin, G. N., Capone, J. I., Veilleux, S., Moseley, S. H., Gehrels, N. A., and Vogel, S. N., "Detector driver systems and photometric estimates for RIMAS," in [*Ground-based and Airborne Instrumentation for Astronomy V*], Proc. SPIE **9147**, 91472W (2014).

[3] Rauscher, B. J., Lindler, D. J., Mott, D. B., Wen, Y., Ferruit, P., and Sirianni, M., "The Dark Current and Hot Pixel Percentage of James Webb Space Telescope 5 μm Cutoff HgCdTe Detector Arrays as Functions of Temperature," PASP **123**, 953–957 (2011).

[4] Rauscher, B. J., Boehm, N., Cagiano, S., Delo, G. S., Foltz, R., Greenhouse, M. A., Hickey, M., Hill, R. J., Kan, E., Lindler, D., Mott, D. B., Waczynski, A., and Wen, Y., "New and Better Detectors for the JWST Near-Infrared Spectrograph," PASP **126**, 739–749 (2014).

[5] Hinkle, K. H., Wallace, L., and Livingston, W., "Atmospheric Transmission Above Kitt Peak, 0.5 to 5.5 microns," in [*American Astronomical Society Meeting Abstracts*], *Bulletin of the American Astronomical Society* **35**, 1260 (2003).

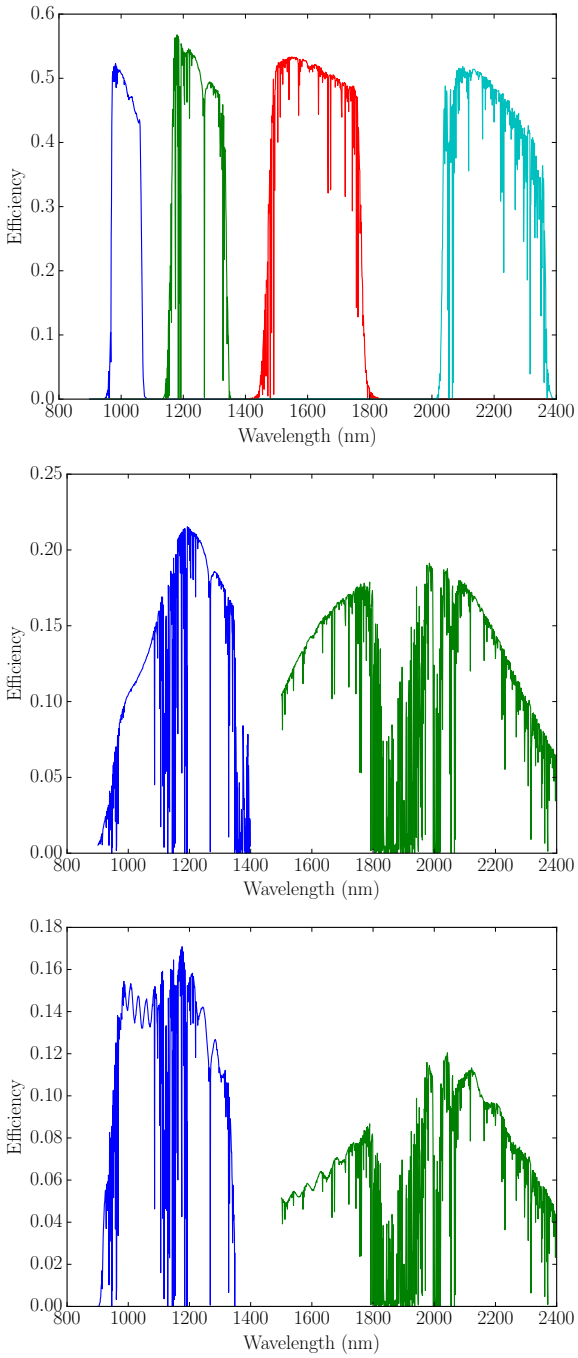

Figure 6. (*top*) Photometric imaging mode effiiencies for YJHK bands. (*middle*) Preliminary low-resolution spectroscopy mode efficiencies. (*bottom*) High-resolution spectroscopy mode efficiencies.